A process-based pore network model construction for granular packings under large plastic deformations

Pedro H C Martins, Marcial Gonzalez

A process-based pore network model construction for granular packings under large plastic deformations

Pedro H. C. Martins[1] and Marcial Gonzalez [*1,2]

[1]School of Mechanical Engineering, Purdue University, West Lafayette, IN 47907, USA
[2]Ray W. Herrick Laboratories, Purdue University, West Lafayette, IN 47907, USA

August 12, 2021

Abstract

We propose a process-based method for constructing a pore network model of granular packings under large deformations. The method uses the radical Voronoi tessellation and constructive solid geometry (CSG) operations on meshes of deformed particles, to construct a three-dimensional solid of the pore network and estimate its geometric characteristics, CTS-model parameters and flow transport properties, and it uses the particle mechanics approach to model consolidation of powders under large deformations. This process-based method thus explicitly simulates not only a packing of grains but also its corresponding consolidation process, which in this work is restricted to powder die compaction up to a relative density close to one (i.e., to die filling, compaction to low porosity, unloading, and ejection). The efficacy of the proposed method is borne out by studying granular packings with the same composition, namely a 50-50 binary mixture of two monodisperse systems comprised by elasto-plastic spheres with bonding strength, but with microstructures which are topologically different, namely a random packing, a bilayer, and core-shell structures. These simulations reveal that topological differences affect the formation and evolution of the pore space statistical signature during consolidation and, therefore, showcase that process-based approaches for constructing PNM are of paramount relevance to understanding architectured granular material systems.

1 Introduction

The quality and performance of many granular products are often related to the transport properties and, in turn, to their interconnected microstructure and pore space. However, the pore space is typically not created by design but rather it is the by-product of the consolidation process imparted by the manufacturing process [1]. A number of consolidation processes are available at industrial scale. In this paper, we restrict attention to powder compaction processes and thus to granular systems under large plastic deformations. It is worth noting that granular pore space does not only evolve during manufacturing but it also evolves during product performance, such as swelling, disintegration and dissolution, which naturally hinders the study and modeling of transport phenomena in granular products [2].

[*]marcial-gonzalez@purdue.edu

A pore-network model (PNM) is an idealized decomposition of the otherwise geometrically complex granular pore space. It aims to preserve the the connectivity, shape and size of the interconnected network. The decomposition procedure identifies individual pores and throats, which are in turn mapped to nodes and edges of the network, respectively. Nodes and throats are then endowed with geometric information relevant to transport phenomena. It bears emphasis that accurate predictions of multiphase flow are entirely dependent on how the local morphology of throats and pores is described, and on how this information is used to estimate transport properties, since pores control imbibition and throats control drainage kinetics [3]. Furthermore, in general, PNM simulations consist of two significant steps, namely construction and flow simulation [2, 3].

The construction of a pore-network model (PNM) can be classified into three methodologies, namely, statistical reconstruction models, direct mapping models, and grain-based or process-based models [2]. The first two methods rely on pore-space imaging techniques, such as (i) x-ray computed micro-tomography (micro-CT) [4, 5, 6], (ii) focused ion beams (FIB) [7, 8, 9] and scanning electron microscopy (SEM) [10], and (iii) nuclear magnetic resonance (NMR) [11, 12]. The fundamental difference between the two image-based methods is that the former is an equivalent pore-network in a statistical sense, whereas the latter is a one-to-one spatial correlation between the porous material and the equivalent pore-network structure [2, 3]. Process-based models explicitly simulate a packing of grains and the consolidation process, such powder compaction, and they are the focus of this paper.

Statistical reconstruction methods directly use two-dimensional microstructural images to create a statistically equivalent three-dimensional network using probability distributions of morphologic parameters retrieved from images [2]. These geometrical properties typically are porosity distribution, i.e., a one-point correlation function, and the probability of finding two points separated by a certain distance within the same phase, i.e., a two-point correlation function, [13, 14]. However, pore-space long-range connectivity is poorly preserved when these low-order correlation functions are derived from two-dimensional images [3]. Notwithstanding, any information can be introduced into an object-based statistical method to improve the reconstruction and preservation of essential morphological properties of the granular material [15, 16]. A case in point is the use of multi-point statistical methods [17, 18, 19, 20, 21, 22].

Direct mapping methods construct a one-to-one mapping between three-dimensional images of real samples and the network model. Three-dimensional images are comprised of a collection of voxels and existing algorithms operate a subset of voxels. For example, the medial axis algorithm, or medial axis skeletonization, iteratively converts any pore-voxel adjacent to a solid into a solid-voxel until a one-voxel wide skeleton of the pore-space is obtained [23, 24, 25, 26]. This skeleton is then a topologically equivalent graph of the three-dimensional pore-space [3]. These algorithms possess several drawbacks. The resultant network is dependent on the order the pore-space is reduced. It may have excessive dead-ends due to roughness and irregularities, an unrealistic number of branches that are nearby each other [27]. Similarly, the maximum ball algorithm identifies pores and throats, instead of computing an equivalent skeleton, by finding large spheres that touch solid surfaces and smaller spheres that connect them. This method also has limitations, and the arbitrary partition of pore-space complicates the identification of pore and throat [2, 3]. It is worth noting that it is also possible to combine both methods, where the maximal ball is used to define pores, and the medial axis is used to define throats [26]. Despite of this and other improvements in the algorithm, direct mapping yields an irregular lattice [28].

Process-based methods explicitly simulate a packing of grains and the consolidation process. These methods have been used by the geoscience and energy-research communities to mimic the sedimentation, compaction, and diagenesis processes by which rocks are formed [29, 30, 31, 32, 33]. Diagenesis is modeled by uniformly swelling particles; however, particle's position and deformation

do not stem from a force equilibrium configuration. Furthermore, these models are typically based on random close packings of spheres [30, 31], which limits the range of particle's morphology to spheroids. The resulting particulate system is then tessellated to obtain pore-space properties and carry out pore-network fluid flow simulations. Despite these limitations, experiments and images obtained from micro-tomography using Fon-tainebleau sandstone [34, 33] and carbonate rock [35], demonstrate that the process-based method is superior in predicting transport properties relative to stochastic models based on one- or two-point correlations functions.

The Delaunay triangulation and its dual graph, the Voronoi tessellation, are the optimal decomposition methods for a monodisperse packing of undeformed spheres, often termed loose spherical packing. The former method divides the envelope volume of porous media into tetrahedra, where each particle's center of mass is a vertex. The latter method divides the pore-space into Voronoi cells, where edges and vertices correspond to throats and pores, respectively. Hence, pore-network features emerge naturally from the tessellation [36].

The regular Delaunay triangulation, also known as weighted Delaunay triangulation, and its dual graph, the radical Voronoi tessellation (also referred to as the Laguerre tessellation), are the optimal decomposition methods for polydisperse spherical packings [37, 36]. Figure 1 demonstrates the effectivity of this decomposition in a two-dimensional polydisperse packing of circular particles with and without overlapping. The method, however, constrains the three-dimensional pore connectivity to four throats only and creates too many unnecessary pores [25, 38]. These limitations are overcome by using merging algorithms [39, 40]. Naturally, these tessellation techniques loose accuracy for non-spherical particles, but algorithms for three-dimensional set Voronoi diagrams of packings of arbitrarily shaped particles exist [41, 42].

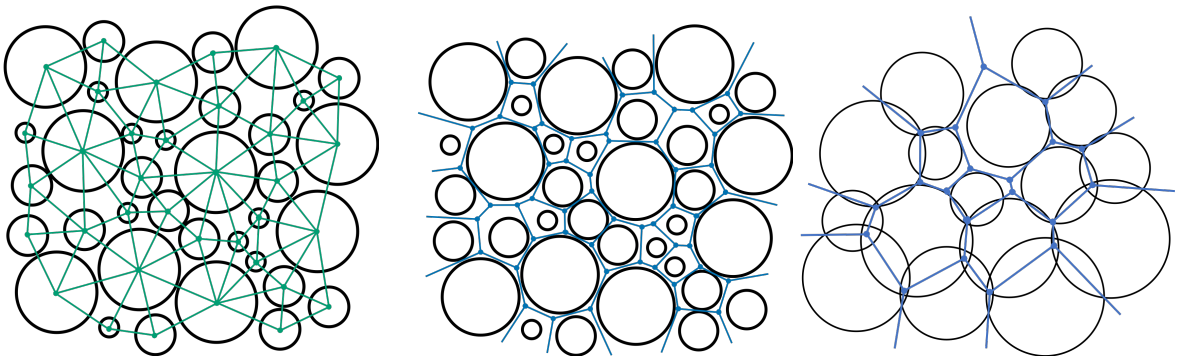

Figure 1: Tessellation of two-dimensional packings. (a) Regular Delaunay triangulation and its dual. (b) Radical Voronoi tessellation of a loose packing. (c) Radical Voronoi tessellation of a packing with overlaps. Figures adapted from [43, 44].

This work presents a process-based method for constructing a pore network model that is applicable to granular packings under large deformations, thus addressing a gap in the literature. It uses the radical Voronoi tessellation [37, 45] and constructive solid geometry (CSG) operations on meshes of deformed particles to construct a three-dimensional solid of the pore network and estimate its geometric characteristics and flow transport properties. The method also uses the particle mechanics approach for modeling the consolidation of powders under large deformations [46, 47, 48, 49, 50]. Figure 2 illustrates the proposed method and its different components. The literature on CSG is vast and the state-of-the-art techniques are classified in incremental [51, 52, 53] and non-incremental

[54, 55, 56] methods. A thorough presentation that encompasses efficiency, computational complexity, memory requirements, topology simplicity, and robustness of several CSG libraries can be found in [55, 56]. Here, we adopt the robust non-incremental method [55]. Flow transport properties are obtained by assuming that the pore network is solely composed of either throats [57, 58, 59] or pores [60] —hybrid models also exist [61, 62]. The shape of each element is next characterized to determine effective capillary pressure, conductance, shape factor, and surface area. Shapes are characterized using (i) simple convex shaped elements, such as the circle-triangle-square (CTS) model [63], (ii) regular star-shaped elements [64, 65], (iii) irregular hyperbolic polygons [66, 67], (iv) n-irregular polygons [68], and (v) half-throat corners [69]. Here, we use the CTS mode to characterize throat elements.

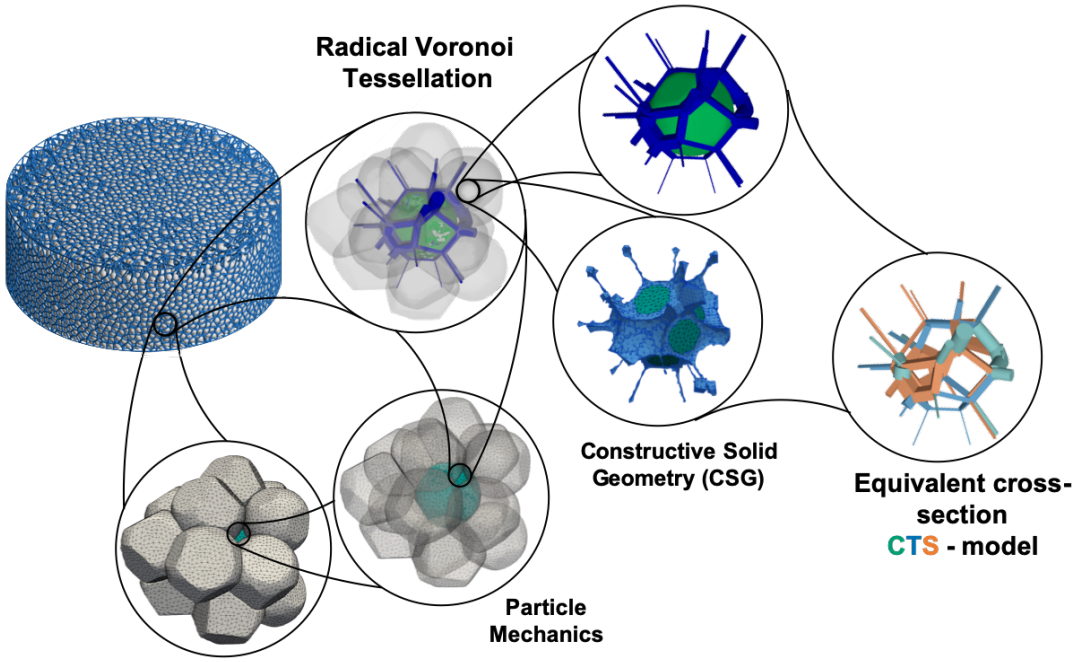

Figure 2: The process-based pore network model construction for granular packings under large plastic deformations is comprised of four key elements: (i) a particle mechanics approach to attain packings consolidated at large deformations, (ii) a tessellation algorithm to build the pore-network topology, (iii) CGS evaluations to generate pore geometry, and (iv) a CTS-model to assign transport properties to the pore network model.

The paper is organized as follows. In Section 2, we briefly introduce the consolidation process of granular packings under large deformations and discuss how contact mechanics can be used as a reversible upscaling method. In Section 3, we propose a process-based pore network model of granular packings under large deformations, and we verify its accuracy at different levels of deformation. In section 4, we map the resultant pore-space geometry to a generalized CTS model and we conduct a statistical characterization of pore space evolution during consolidation of granular packings under large deformations. Next, in Section 5, we study granular packings with the same composition, namely a 50-50 binary mixture of two monodisperse systems comprised by elasto-plastic spheres with bonding strength, but with microstructures which are topologically different, namely a random packing, a bilayer, and core-shell structures. Finally, concluding remarks are collected in Section 6.

2 Consolidation of granular packings under large deformations

Process-based or grain-based methods explicitly simulate not only a packing of grains but also its corresponding consolidation process. In this paper, we restrict attention to powder compaction processes and, in this section, we present the particle mechanics approach used for modeling the consolidation of powders under large deformations. Specifically, powder die compaction encompasses four stages, namely die filling, compaction, unloading, and ejection, as exemplified in Figure 3. At the particle scale, this consolidation process typically consists of several steps, that is of filling the cavity formed by two punches and a die, packing rearrangement, particle elastic deformation, brittle fracture or plastic deformation, or both, and formation of inter-particle solid bridges [70, 71, 50]. It is indeed these dissipative and irreversible processes that ultimately give rise to compact formation inside the die and, in this work, we focus on elasto-plastic behavior, with formation of solid bridges, and do not consider brittle fracture—which is relevant to many industries, manufacturing processes and materials systems, such as the manufacturing of pharmaceutical solid tablets and the use of ductile, amorphous polymers for excipients (see [50] and references therein).

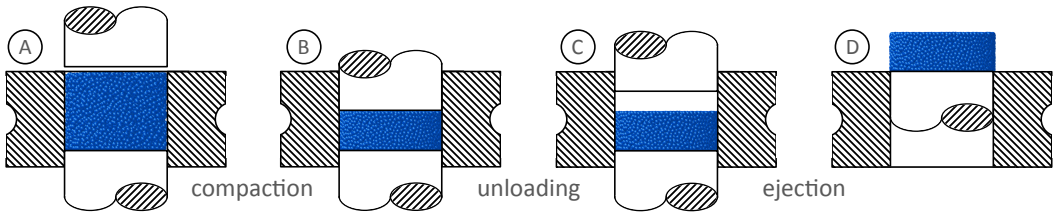

Figure 3: Consolidation of the granular packing during the stages of die compaction: (A) die filling, (B) compaction, (C) unloading, and (D) tablet ejection. Adapted from [50].

We carry out three-dimensional particle mechanics static calculations to predict microstructure formation and evolution during compaction, unloading, and ejection (see Figure 3). For simplicity, powder morphology and size distribution are simplified to monodispersed packings of spherical particles. Generalized loading-unloading contact laws for elasto-plastic spheres with bonding strength are employed to describe inter-particle interactions [50]. Hence, a sequence of static equilibrium configurations are used to simulate consolidation of granular packings under large deformations [47], and these deformed packings will be used to evaluate pore-network formation and evolution during compaction. Specifically, we simulate a granular system comprised of 39,914 weightless spherical particles with radius $R = 125$ μm, inside a rigid cylindrical die of diameter $D = 10$ mm and between two flat rigid punches, as shown in Figure 4.

The granular bed is created using a random particle sequential addition method. This method consists of dropping particles one by one in a gravitational field and, using kinematics laws only for interparticle interactions, that is dropping and rolling rules, finding a stable position in contact with three other previously packed particles [72]. It is worth noting that the initial particle arrangement plays a role in defining the jamming point and compaction response at small forces or deformations. The description of the die filling process can be improved by, for example, adopting dynamic laws, rather than kinematic rules [73, 74]. However, the investigation of these effects is beyond the scope of this work.

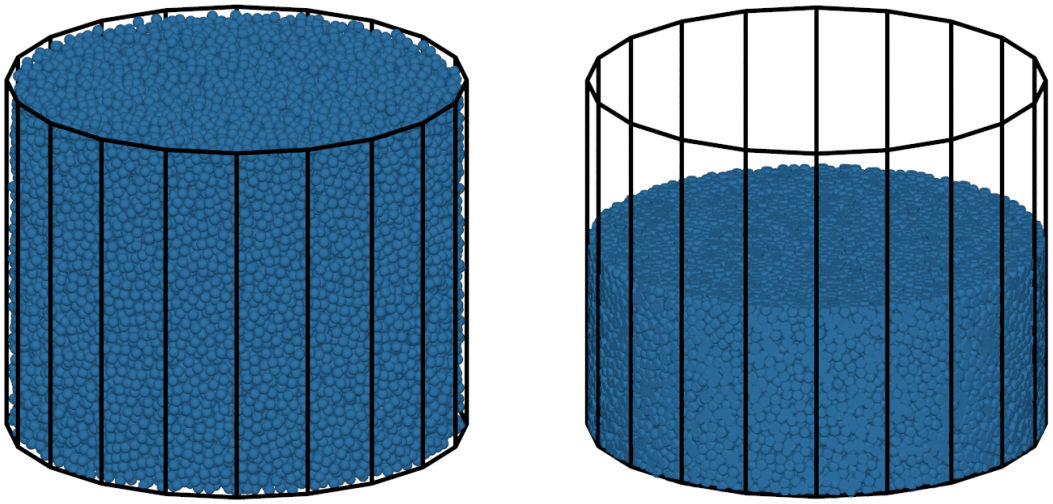

(a) (b)

Figure 4: Compacted granular bed comprised of 39,914 weightless spherical particles, with Young's modulus $E = 5$ GPa, Poisson's ratio $\nu = 0.25$, hardening stiffness $\kappa = 150$ MPa, hardening exponent $m = 2$, and fracture toughness $K_{Ic} = 1.26$ MPa m$^{1/2}$: (a) before compaction at a relative density, or solid fraction, of 0.5219, and (b) after compaction to a relative density of 0.9521.

2.1 Contact mechanics as a reversible upscaling method

Mechanistic contact laws are built as an analytical upscaling of continuum contact mechanics, that is, under the kinematic constraint of no material interpenetration, displacement, strain and stress fields are upscaled to a relative position between the deformable bodies, a pressure distribution at the contact interface, and an effective contact force. Hertz contact law and the nonlocal contact formulation developed by Gonzalez and co-workers [46, 75] are examples of a local and a nonlocal contact law for spherical elastic particles. Similarly, local plastic contact laws for spherical particles with [50] and without [76] result from an analytical upscaling of continuum contact mechanics and the assumption of rigid-plastic power law hardening behavior. If the interacting particles have different plastic properties, it is worth noting that contact surface is not flat and that sinking-in or piling-up regimes may dominate the free surface in the vicinity of the contact interface—see, for example, [76] for the interaction between a plastic sphere and a rigid plane. Regardless of these features in the plastically deformed bodies, the deformation field fulfills the classical assumption of incompressibility for bodies with no internal porosity.

The particle mechanics approach described above allows to determine relative position between particles and interparticle contact forces, without having to solve for diplacement, strain and stress fields from the continuum contact mechanics problem. However, under the assumption of flat and circular contact interfaces and, thus, for pair of spherical particles whose radii and plastic properties are not significantly different, the position of the contact plane can be approximated from geometric considerations and material interpenetration constraints. Furthermore, the displacement field of the spherical surface can be estimated from these contact planes and the incompressibility constraint. Therefore, we propose an algorithm to reverse the upscaling intrinsic to any mechanistic contact law and, hence, estimate the deformed configuration of a solid spherical particle from the relative position with its neighbors and the incompressibility constraint of plastic deformations. This algorithm in shown in 1 and it uses (i) a mesh $\mathbf{PM}_i$ to discretize the i-th particle, (ii) a simple projection of all mesh

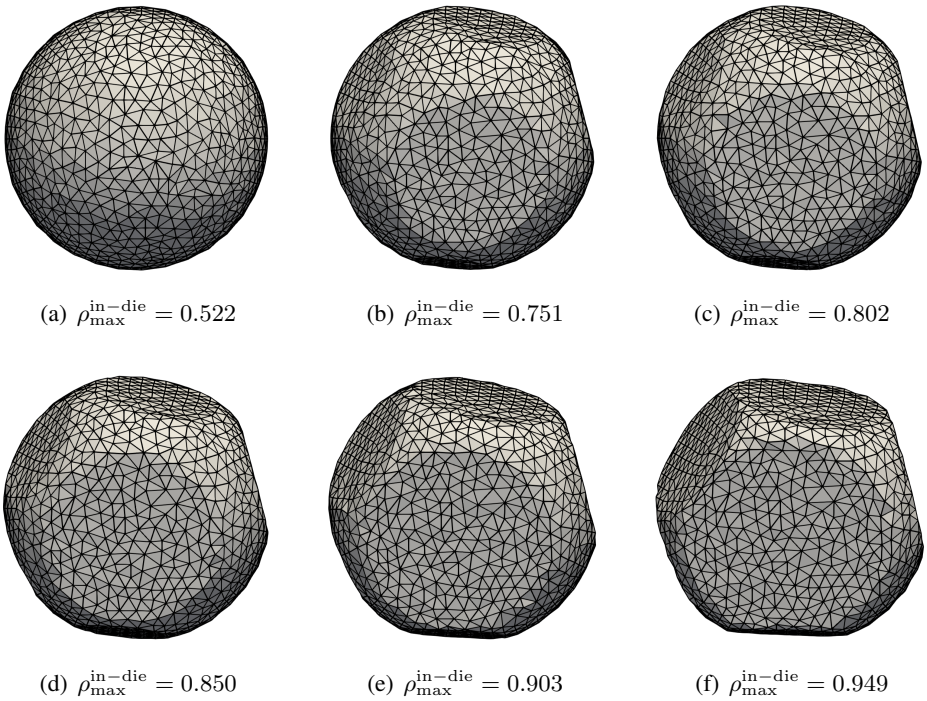

(a) $\rho_{\max}^{\text{in-die}} = 0.522$ (b) $\rho_{\max}^{\text{in-die}} = 0.751$ (c) $\rho_{\max}^{\text{in-die}} = 0.802$

(d) $\rho_{\max}^{\text{in-die}} = 0.850$ (e) $\rho_{\max}^{\text{in-die}} = 0.903$ (f) $\rho_{\max}^{\text{in-die}} = 0.949$

Figure 5: Deformed configuration of an arbitrarily selected particle, as the granular bed is deformed at different in-die relative densities, namely $\rho_{\max}^{\text{in-die}}$ = [0.522, 0.751, 0.802, 0.850, 0.903, 0.949]. The granular bed and corresponded material properties are shown in Figure 4.

nodes outside the contact plane back onto the contact interface to prevent material interpenetration, and (iii) a bisection procedure to enforce volume preservation. For a loose packing in equilibrium, interparticle contact points lie on the face of the Voronoi face shared by neighbor particles. For flat contact interfaces, i.e., for interfaces between particles of equal size and properties [77], the face of the Voronoi cell shared by neighbor particles is accurately located at the contact interface, i.e., at the intersection of the undeformed particle-particle pair or undeformed particle-wall pair. For non-flat contact interfaces, the location of the Voronoi face only serves as a first-order approximation of the location of the contact interface, which can be further improved by adapting the projection procedure to accommodate for the resulting curved contact interface [77]. Furthermore, a corollary of this algorithm is that all surfaces outside the contact interface have the same curvature. These observations are evidence that the algorithm gives a first-order approximation of the deformed configuration, and the implementation of the suggested improvements is beyond the scope of this paper. Lastly, the surface area and volume are readily available from the resultant mesh and, as it is illustrated in the next section, the pore network can be estimated. Figure 5 illustrates the deformed configuration of an arbitrarily selected particle, as the granular bed is deformed at different in-die relative densities, or solid fractions.

Algorithm 1 Algorithm for generating deformed particles

procedure DEFORMEDPARTICLE($\mathbf{x}, \mathbf{R}, \mathcal{N}, \mathrm{TOL}, \mathrm{SMAX}$)
  for $i = 1 : N$ **do** ▷ loop over particles
    $V_i \leftarrow (4/3)\,\pi R_i^3$ ▷ reference particle volume
    $R_a \leftarrow 0.5R_i$ and $R_c \leftarrow 5.0R_i$ ▷ radii bounds of bisection interval
    $\mathbf{PM}_a \leftarrow \mathrm{sphereMesh}(\mathbf{x}_i, R_a)$ ▷ scale mesh of particles a and c
    $\mathbf{PM}_c \leftarrow \mathrm{sphereMesh}(\mathbf{x}_i, R_c)$
    for $j = \mathcal{N}_i$ **do** ▷ loop over neighbors
      $[\mathbf{n}, \mathbf{x}_n] \leftarrow \mathrm{contactPlane}\,(\mathbf{x}_i, \mathbf{x}_j, R_i, R_j)$ ▷ find contact plane $[\mathbf{n}, \mathbf{x}_n]$
      $\mathbf{PM}_a \leftarrow \mathrm{projectPoints}\,(\mathbf{PM}_a, \mathbf{n}, \mathbf{x}_n)$ ▷ project points back onto plane
      $\mathbf{PM}_c \leftarrow \mathrm{projectPoints}\,(\mathbf{PM}_c, \mathbf{n}, \mathbf{x}_n)$
    end for
    $V_a \leftarrow \mathrm{volume}\,(\mathbf{PM}_a)$ and $V_c \leftarrow \mathrm{volume}\,(\mathbf{PM}_c)$ ▷ volume of deformed particles
    $S \leftarrow 1$
    while $S \leq \mathrm{SMAX}$ **do**
      $R_b = 0.5(R_a + R_c)$
      $\mathbf{PM}_b \leftarrow \mathrm{sphereMesh}(\mathbf{x}_i, R_b)$ ▷ mesh of particle i
      for $j = \mathcal{N}_i$ **do** ▷ loop over neighbors
        $[\mathbf{n}, \mathbf{x}_n] \leftarrow \mathrm{contactPlane}\,(\mathbf{x}_i, \mathbf{x}_j, R_i, R_j)$ ▷ find contact planes $[\mathbf{n}, \mathbf{x}_n]$
        $\mathbf{PM}_b \leftarrow \mathrm{projectPoints}\,(\mathbf{PM}_b, \mathbf{n}, \mathbf{x}_n)$ ▷ project points back onto plane
      end for
      $V_b \leftarrow \mathrm{volume}\,(\mathbf{PM}_b)$ ▷ deformed particle volume
      if $\|V_b/V_i - 1\| \leq \mathrm{TOL}$ **then Break while** ▷ bisection algorithm
      else if $\mathrm{sgn}(V_b - V_i) = \mathrm{sgn}(V_a - V_i)$ **then** $R_a \leftarrow R_b$ and $V_a \leftarrow V_b$
      else $R_c \leftarrow R_b$ and $V_c \leftarrow V_b$
      end if
      $S \leftarrow S + 1$ ▷ increase step counter
    end while
    $\mathrm{store}(i, \mathbf{PM}_b)$ ▷ store i-th particle mesh for CSG algorithm
  end for
end procedure

3 Process-based pore network model of granular packings under large deformations

A pore-network model (PNM) is an idealized decomposition of the otherwise geometrically complex granular pore space. It aims to preserve the topology, shape and size of the interconnected network [3], which is typically discretized into pores (i.e., the regions of pore space furthest from the solid domain) and throats (i.e., the more constricted regions of the pore space that connect the pores). Since the former control imbibition and the latter control drainage kinetics, an accurate description of pores, throats, and their interconnectivity are needed.

3.1 Radical Voronoi tessellation of the granular pore space

The weighted Delaunay triangulation (wDT) and its dual graph, the radical Voronoi tessellation (rVRT), are the optimal decomposition methods for polydisperse spherical packings. For example, by using the square of the particle radius as the weight [78], Figures 1(b) and 1(c) are obtained for two-dimensional packings. In this work, we use the open-source tessellation code Voro++ (v. 0.4.6) [45]. It carries out cell-based calculations to compute the Voronoi cell complex for each particle individually, rather than a global network of vertices and edges. A cell complex X_i is a collection of vertices (0-cells), edges (1-cells), faces (2-cells), and volumes (3-cells), i.e., the collection of sets $E_0(X_i)$, $E_1(X_i)$, $E_2(X_i)$ and $E_3(X_i)$, respectively. Voro++ locally generates regular cell complexes, i.e., for each particle i characterized by a 0-simplex B_i in the wDT, it generates a finite collection of disjoint open cells that fit together conformingly and whose union is X_i, such that the 0-simplex B_i is the dual of the one single 3-cell in $E_3(X_i)$—i.e., such that $B_i = \mathrm{Dual}(E_3(X_i))$. In the context of a PNM, vertices of the rVT are pores, and edges are throats. The set of all $E_3(X_i)$ is globally labeled by Voro++, since particles or 0-simplices B_i of the wDT are globally labeled. Pores and throats, or 0-cells and 1-cells, however, have as many labels in Voro++ as particles surrounding them. This multiplicity has to be removed before building a PNM.

We remove the multiplicity of vertices and edges to generate the PNM's set of unique pores and throats, respectively, by utilizing topological operators [79] readily available in Voro++. Specifically, we use the following dual operation between the rVT and the wDT

$$\mathrm{Dual}(\delta_j) \rightarrow \{B_k, B_q\} \tag{1}$$

where δ_j is a 2-cell in the rVT and set $\{B_k, B_q\}$ represents a 1-simplex in the wDT, and we construct

$$\mathrm{Dual}(\upsilon_j) \rightarrow \{B_k, B_q, B_r, B_s\} = \bigcup_{\delta_m \in \mathrm{I}_2(\upsilon_j)} \mathrm{Dual}(\delta_m) \tag{2}$$

where υ_j is a 0-cell in the rVT and the quadruplet $\{B_k, B_q, B_r, B_s\}$ represents a 3-simplex in the wDT. In the above equation $\mathrm{I}_2(\upsilon_j)$ is the set of 2-cells incident to the 0-cell υ_j, which is readily but locally available in the one single cell complex $X_i \ni \upsilon_j$ generated by Voro++. The union operation eliminates duplicates and the cardinality of the resulting set is 4, for any primal-dual pair (wDT , rVT). Next, we eliminate any multiplicity of vertices υ_j which have the same quadruplet as dual and, thus, relabel the 0-cells throughout the rVT to identify the set $\mathbf{P}$ of unique pores, and corresponding neighbors $\mathbf{PN} = \mathrm{Dual}(\mathbf{P})$, in the PNM . Similarly, the set $\mathbf{T}$ of unique throats, or 1-cells $\{\upsilon_m, \upsilon_n\}$, is identified by eliminating any multiplicity of duplets, and the corresponding neigbors is obtained as $\mathbf{TN} = \mathrm{I}_3(\mathbf{T})$, where the set of 3-cells incident to the 1-cell $\{\upsilon_m, \upsilon_n\}$ is given by

$$\mathrm{I}_3(\{\upsilon_m, \upsilon_n\}) \rightarrow \{B_k, B_q, B_r\} = \mathrm{Dual}(\upsilon_m) \bigcap \mathrm{Dual}(\upsilon_n) \tag{3}$$

In the above equation, for simplicity, 3-cells are represented by their corresponding dual 0-simplices. The intersection operation results in a set of cardinality 3, for any primal-dual pair (wDT , rVT).

3.2 Pore space construction using constructive solid geometry (CSG) methods

A porous media is defined by a solid matrix and its pore space, which may be occupied by a multiphase gas-liquid system. The total volume of a porous material system V is then described by the volume of the solid matrix $V_{\rm s}$ and the volume of the pore space $V_{\rm p}$ which, in turn, can be decomposed into gas-liquid phases. For example, the pore space of a two-phase flow problem is decomposed into a wetting phase of volume $V_{\rm w}$ and a non-wetting phase of volume $V_{\rm nw}$, such that $V = V_{\rm s} \cup V_{\rm p} = V_{\rm s} \cup V_{\rm w} \cup V_{\rm nw}$ and $V_{\rm s} \cap V_{\rm p} = V_{\rm s} \cap V_{\rm w} \cap V_{\rm nw} = \emptyset$. The total porosity of a porous media is defined as the fraction $V_{\rm p}/V$, and the effective porosity is given by the pore-space that is effectively interconnected. A medium is permeable if the effective porosity is larger than zero [3] and pore-network fluid flow simulations can only be carried out in permeable porous media.

The effective geometric properties of the elements in a pore-network model can be computed from the following four parameters: the cross-section area of each throat A_t, the length of each throat or the distance between two pores L_t, the surface area of each throat in contact with the fluid S_t, and the volume of each throat V_t. Details of the cross-section polygonal shape may be used, but it tends to be extremely irregular. The distance between pores L_t is given by the length of the edges of the rVT. We describe next the procedure developed to estimate cross-section area, surface area, and volume using constructive solid geometry (CSG) methods.

A complex solid geometry can be constructed by sequential evaluation of CSG boolean operations between pairs of polygon meshes, such as union, intersection, difference, and symmetric difference. Therefore, the volume, V_t and surface areas, S_t and A_t, of elements of the decomposed pore space are calculated from resultant meshes. Before proceeding with the boolean operations, we define a reference geometry $\mathbf{TM}$ for the pore-space element that preserves the porous media total volume and that, after CSG evaluations, it results in a tessellation of the pore space. The natural choice for $\mathbf{TM}$ is the set of 3-simplices in the wDT and, specifically, for each pore-element the two 3-simplices or tetrahedra that are dual of the two vertices forming a throat or edge in the rVT. Figure 6 shows this sequential procedure between $\mathbf{TM}$ and the mesh of the three surrounding deformed particles characterized by meshes $\mathbf{PM}_1$, $\mathbf{PM}_2$ and $\mathbf{PM}_3$. The volume V_t is then computed by the resultant mesh, and the cross-section area A_t is measured on the plane where the two tetrahedra meet, i.e., the plane defined by the 0-simplices in the wDT associated to the three particles. Similarly, the surface area S_t is estimated as half the area of the body given by the intersection between the pore-element mesh and each neighboring particle slightly dilated mesh (see Figure 7). It is worth noting that none of these operations are different for neighbors comprised of die/punch walls or compact free surfaces.

In this work, we use the gptoolbox library [80], which is available as a MATLAB toolbox that uses CGAL [53] and LibiGL [55], to evaluate all boolean operations. We use the MatGeom toolbox [81] to compute geometric properties of meshes, such as volume, surface area, plane mesh intersection, and normal vectors. It is worth noting that the algorithm described in this section is embarrassingly parallelizable since each pore element is entirely independent from each other.

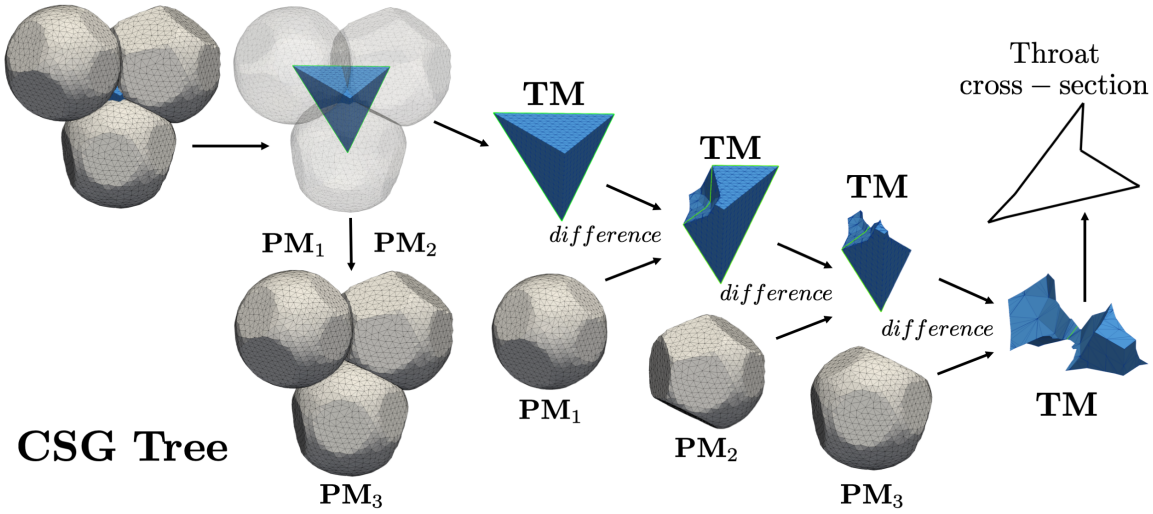

Figure 6: CSG tree for determining throat volume V_t and cross-section area A_t.

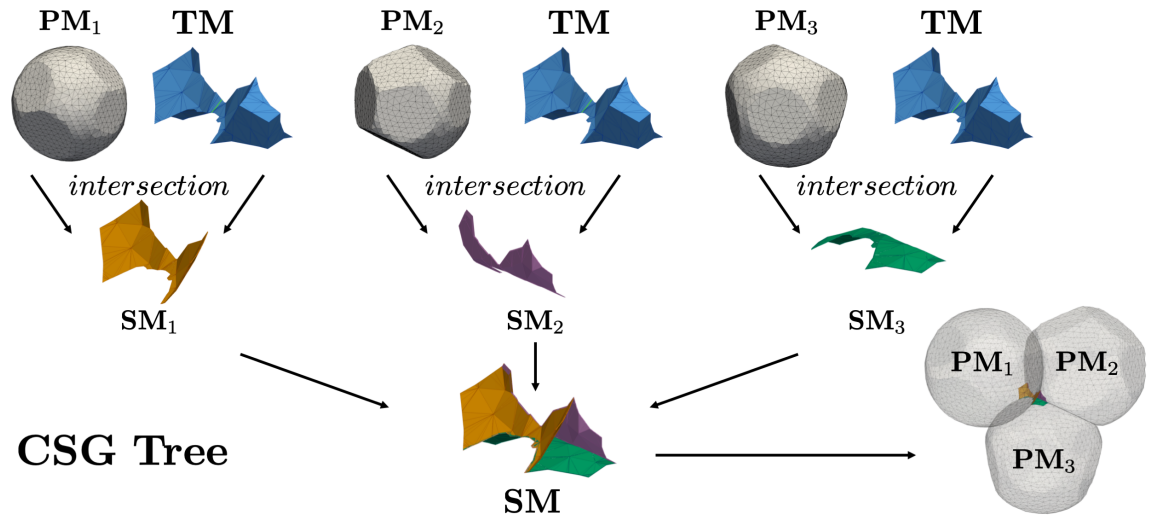

Figure 7: CSG tree for determining throat surface area S_t.

3.3 Verification of the pore space construction

The pore network construction is solely based on the geometry of the deformed granular packing, and the deformed equilibrium configuration in turn depends on the mechanical properties of the particles and on the consolidation process. Therefore, we verify correctness of the proposed construction algorithm in estimating pore space volume and surface by using unconsolidated or loose spherical packings, since they are amenable of analytical pore space volume and surface calculations by virtue of the undeformed nature of the particles. We also verify correctness in volume estimation throughout the consolidation process, that is at packing plastically deformed at different densities, since plastic flow is assumed isochoric (see Section 2.1). Specifically, we use monodisperse and polydisperese systems comprised of $39,914$ and $51,693$ spherical particles, respectively, in a cylindrical container with diameter $D = 5.4$ mm and $D = 2.84$ mm, respectively. Particles in the monodisperse packing

have a radius of $R = 125$ μm. The polydisperse system corresponds to a truncated packing of Lactose monohydrate with mean radius of $\bar{R} = 77.72$ μm, and values ranging from 44 μm to 399 μm [82].

The verification is performed using a mesh size of $R/3000 \approx 40$ nm in the algorithms presented in Sections 2.1 and 3.2. Results for loose polydisperse and monodisperse systems, presented in the first two rows of Table 1, indicate that both volume and surface area are conserved. For consolidated packings, it is worth noting that the relative error in volume conservation increases with packing relative density. This behavior is rooted at the lack of a non-local contact formulation for plastic particles (cf. non-local contact formulation for elastic particles [46, 75]) and, thus, of a good estimation of the deformed configuration at high levels of confinement (i.e., the construction algorithm presented in Section 2.1 becomes increasingly inaccurate at higher levels of confinement). Similarly, the table does not present surface area results for consolidated packings, due to the lack of analytical expressions for the displacement field of a deformed and confined particle.

Table 1: Verification of the pore space construction.

Packing Information		Relative Error [%]				
	Relative Density	Solid Matrix Volume	Solid Matrix Surface Area	Pore-Space Volume	Pore-Space Surface Area	Tablet Total Volume
Polydisperse	0.539	0.029	0.282	-0.090	1.191	-0.035
Monodisperse	0.520	0.016	0.196	-0.644	0.931	-0.301
Monodisperse (consolidated)	0.751	-0.060	–	-1.217	–	-0.348
	0.802	-0.077	–	-1.306	–	-0.320
	0.850	-0.176	–	-0.536	–	-0.230
	0.903	-0.698	–	-6.516	–	0.053
	0.949	-1.849	–	-43.966	–	0.495

4 Generalized CTS pore network model

A generalized pore network model is based on the partitioning of the pore space into a representative nexus of pores and throat elements that uphold connectivity and on their related flow properties. Pore connectivity is given by the number of throats elements connected to a given pore element, whereas flow properties are related to geometrical information of the pore-space elements. This representation allows in turn to model flow anisotropy in porous media. However, reliable predictions require an accurate description of the local geometry [3] and, in particular, of the equivalent cross-section of each pore-space element. For example, the CTS model maps each pore into a channel with either circular, triangular, or squared cross-section. This classification is based an analogy between the shape factor of a pore-space element and of a straight channel. For a straight channel, the shape factor G is defined as the ratio between cross-sectional area and perimeter squared, i.e., as $G = A/P^2$. However, for a pore-space element $\mathbf{TM}$, the following shape factor definition is adopted in this work

$$G(\mathbf{TM}) := G(L_t, V_t, S_t) = \frac{L_t\, V_t}{S_t^2} : \begin{cases} \mathbf{TM} \mapsto \bigcirc, & \text{if } G \geq 1/4\pi \\ \mathbf{TM} \mapsto \triangle, & \text{if } 1/4\pi < G \leq \sqrt{3}/36 \\ \mathbf{TM} \mapsto \square, & \text{otherwise} \end{cases} \tag{4}$$

where L_t is the distance between pores, V_t is the element volume, and S_t is the solid surface area [63]. The mapping is not unique for scalene triangles and, thus, we adopt an heuristic method that preserves the value of G [83, 63]. Figure 8 depicts the pore-space element geometric parameters, the pore space surrounding a particle, and the equivalent CTS model.

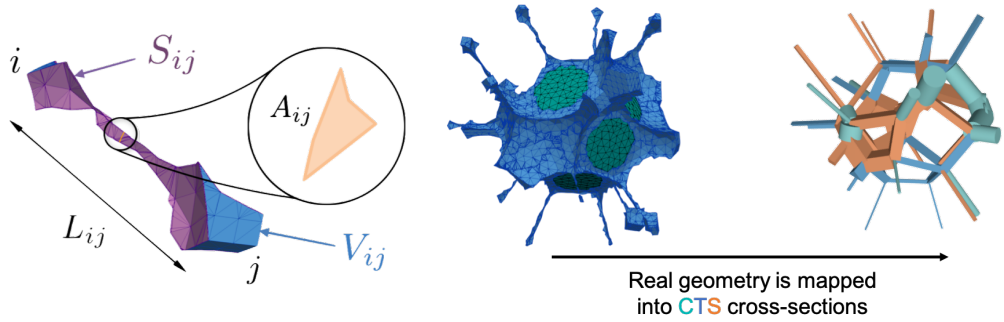

(a) (b)

Figure 8: (a) Pore-space element geometric parameters, namely the throat cross-section area A_t, length L_t, surface area in contact with fluid S_t, and volume V_t. (b) Pore space (in blue) surrounding a particle (in green), and the equivalent CTS model.

The equivalent conductance K of a pore-space element also depends on the cross-sectional shape, pore-space dimensions and fluid viscosity μ [84, 83, 63]. In this work, we adopt a definition [36] compatible with the Kozeny–Carman [85] derivation of permeability in porous material, that is

$$K_{\bigcirc} = \frac{1}{2}\frac{A_t\, V_t^2}{\mu\, S_t^2} \qquad K_{\square} = 0.5623\frac{A_t\, V_t^2}{\mu\, S_t^2} \qquad K_{\triangle} = \frac{3}{5}\frac{A_t\, V_t^2}{\mu\, S_t^2} \tag{5}$$

which is based on the shape factor defined in equation (4).

It bears emphasis that different shape factor and conductance models offer different approximations of the pore space and, naturally, the estimation of capillary pressure [3]. This geometric approximation is illustrated a rich body of literature on the subject (see, e.g., [64, 65, 66, 67]) and in Figure 9 for the case study presented in Section 2. It is evident form the figure that the cross-section of a pore-space element may be concave [64], while the CTS model only considers three convex geometries, i.e., a circle, a triangle and a square. The adoption of a pore network model that does not have this limitation is beyond the scope of this work.

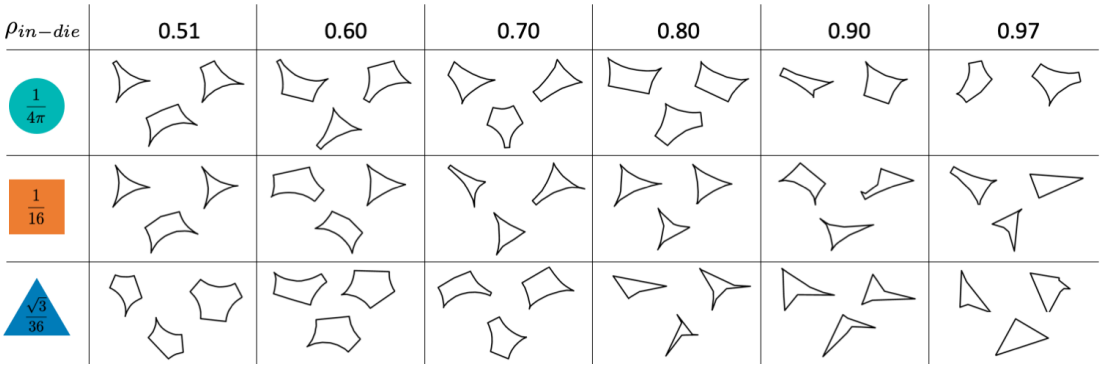

Figure 9: Examples of arbitrarily selected cross-sections that illustrate the CTS model mapping and the evolution of pore network properties during consolidation of granular packings under large deformations.

4.1 Statistical characterization of pore space evolution during consolidation of granular packings under large deformations

The process-based pore network model construction proposed in this paper enables the statistical characterization of pore space evolution during consolidation of granular packings under large deformations. For the monodispersed packings under die-compaction, unloading, and ejection presented in Section 2, that is for a granular bed comprised of 39,914 weightless spherical particles with radius $R = 125$ μm, Young's modulus $E = 5$ GPa, Poisson's ratio $\nu = 0.25$, plastic hardening stiffness $\kappa = 150$ MPa, hardening exponent $m = 2$, and fracture toughness $K_{Ic} = 1.26$ MPa m$^{1/2}$ (see Figure 4), it is observed that the number of pores and throats slightly increases with increasing compaction (see Table 2), due to an increase in neighboring particles during consolidation. The number of pores and throats also change upon unloading and ejection, but it constitutes a negligible change. In conclusion, the topology of the pore space is not sensitive to the reduction in porosity at high levels of confinement.

Table 2: Evolution of pores and throats counts during consolidation of granular packings under large deformations.

$\rho_{\max}^{\text{in-die}}$	After Loading		After Unloading		After Ejection	
	Pores	Throats	Pores	Throats	Pores	Throats
0.751	246,298	492,541	246,588	493,129	246,606	493,150
0.805	246,391	492,767	246,659	493,254	246,667	493,287
0.854	246,522	493,009	246,755	493,467	246,809	493,581
0.904	246,679	493,323	246,983	493,906	246,998	493,946
0.952	247,153	494,277	247,470	494,892	247,508	494,954
0.998	247,670	495,284	247,966	495,900	247,953	495,873

In sharp contrast, the shape and size of the interconnected network elements change significantly with increasing compaction. Figure 10 shows that at relative densities close to the jamming point (e.g., 0.741) most pore elements are classified as circles by the CTS model, whereas at relative densities close to full compaction (e.g., 0.939) most pore elements are classified as triangles, while the percentage of squares does not comparatively change during consolidation and remains around 20-25% of the total number of throats. As expected, circular cross-sections are predominant in loose powders, while triangular cross-sections dominate the shape distribution of highly compacted powders. Furthermore, it is observed that the pore-space topology and shape is established during compaction, and it does not significantly change upon unloading and ejection of the compact. Therefore, we study the evolution of pore-space statistical signature during consolidation solely using microstructures that have been ejected from the rigid die after compaction at a given in-die peak relative density $\rho_{\max}^{\text{in-die}}$.

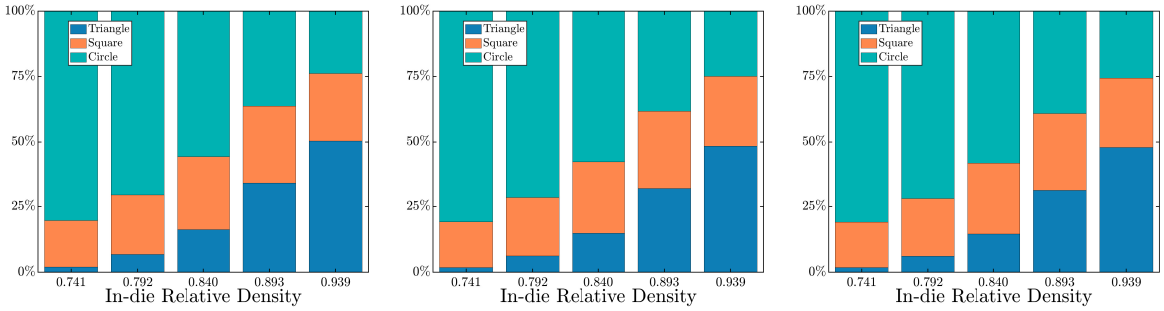

(a) At peak compaction force. (b) After unloading. (c) After ejection.

Figure 10: Evolution of pore-element equivalent shape during consolidation of granular packings under large deformations.

Figure 11 compiles the evolution of the pore-space statistical signature during consolidation. It shows the probability density function[1] of the pore-elements length, surface area, volume, cross-section area and shape factor, at five different in-die relative densities. The first four values are normalized by equivalent dimensions of the particles, i.e., by $\bar{D}_p = 2R$, $\bar{S}_p = 4\pi R^2$, $\bar{V}_p = 4\pi R^3/3$, $\bar{A}_p = \pi R^2$, respectively. It is evident from the figure that as consolidation or relative density increase, (i) the distribution of surface area and shape factor become narrower and skewed towards small values, (ii) the distribution of length does not significantly change, (iii) the distribution of cross-sectional area remains wide, spanning two orders of magnitude, and it shifts towards small values, and (iv) the distribution of volume becomes increasingly skewed and shifted towards small values and it spans two orders of magnitude. It is also interesting to observe that the distribution of surface area becomes bimodal as relative density increases, due to the presence of bounded and unbound pore-elements in the microstructure—a pore-element is bounded if all three incident particles are in contact, and it is unbounded otherwise. In contrast, the distribution of shape factor changes from bimodal to single mode as the relative density increase, showing that triangular cross-section dominate the distribution.

[1]The bin size k_{bin} is given by the following expression which is suitable for non-normal data

$$k_{\text{bin}} = 1 + \log_2(n) + \log_2\left(1 + \frac{\gamma_1}{\sqrt{6(n-2)/(n+1)(n+3)}}\right)$$

where γ_1 is the 3^{rd}-moment-skewness of the distribution, and n is size of the population [86].

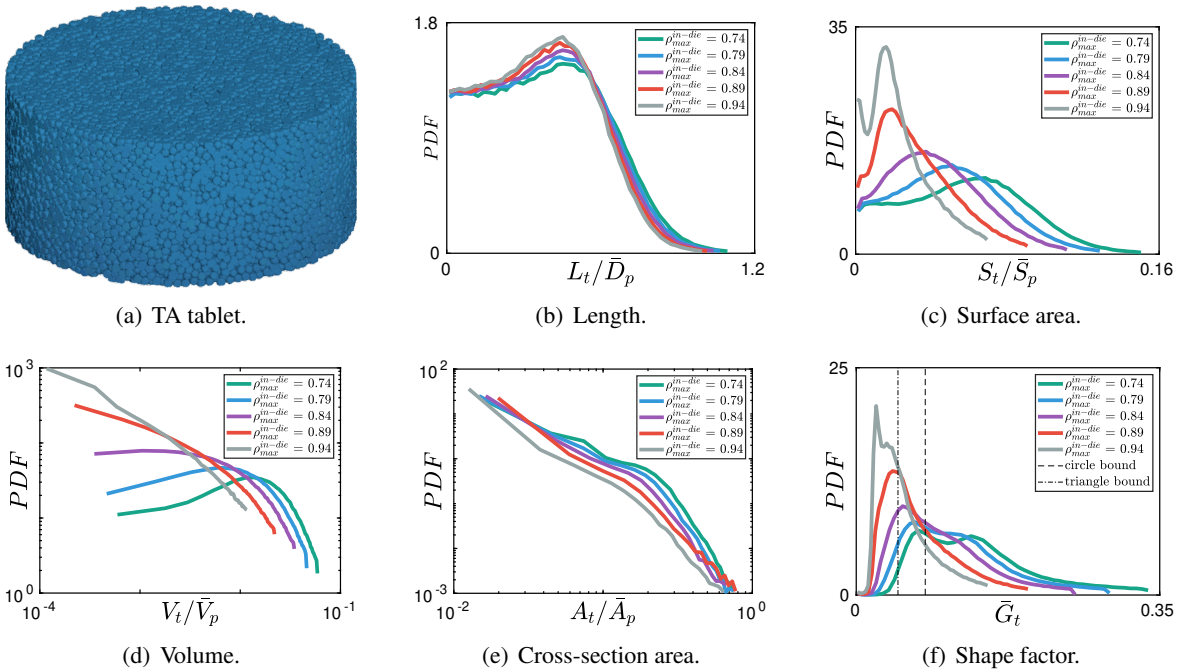

(a) TA tablet. (b) Length. (c) Surface area.

(d) Volume. (e) Cross-section area. (f) Shape factor.

Figure 11: Pore-space statistical signature of the TA tablet.

5 Pore space evolution in topologically different granular mixtures under large plastic deformations

We bear out the efficacy of the proposed process-based pore network model construction using granular packings with the same composition, namely a 50-50 binary mixture of two monodisperse systems, but with microstructures which are topologically different, namely a random packing, a bilayer, and core-shell structures. Bilayer pharmaceutical tablets [49], as well as other complex-configuration dosage forms such as core-shell structures, have gained popularity in recent years to address the need of fixed dose combinations for the treatment of type 2 diabetes, hypertension, pain and HIV/AIDS to mention a few (see, e.g., [87] and references therein). In this section, we specifically investigate granular systems comprised of 19,957 weightless spherical particles with $R = 125$ μm and made of material A, and 19,957 particles with $R = 125$ μm and made of material B. Mechanical properties correspond to lower and upper bounds for many pharmaceutical powders encounter in formulations [50, 88, 89] and they are listed in Table 3, where material A is the same material used in Sections 2 and 4. Pore space formation and evolution during compaction, unloading, and ejection (see Figure 3) is then estimated by carrying out three-dimensional particle mechanics static calculations.

Specifically, we first study two monodisperse packings to establish a baseline, namely tablet TA composed of 100% of material A and tablet TB composed of 100% of material B. In addition, we study a 50-50 random mixture (tablet TRAB), a 50-50 bilayer (THAB), a 50-50 core-shell structure with material A as the core (TCASB), and a 50-50 core-shell structure with material B as the core (TCBSA). Table 4 shows all six formulations and depicts their corresponding cross-section at in-die density of $\rho_{\max}^{\text{in-die}} = 0.952$. We next investigate the evolution of punch and die-wall pressures, internal distribution of relative density or porosity, statistical features of the pore space, and the resulting effective permeability, of all six tablets during their consolidation process.

Table 3: Material properties.

	Elastic Deformation		Plastic Deformation		Bonding & Fracture
	E [GPa]	ν	κ [MPa]	m	K_{Ic} [MPa m$^{1/2}$]
Material A (■)	5	0.25	150	2.00	1.26 $\left(\omega = 150 J/m^2\right)$
Material B (■)	30	0.25	900	2.00	6.19 $\left(\omega = 600 J/m^2\right)$

Table 4: Cross-section, at $\rho_{\max}^{\text{in-die}} = 0.952$, for six different formulations studied.

Single Material		Random Mixture	Structured Mixture		
TA	TB	TRAB	THAB	TCASB	TCBSA
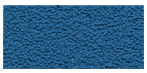	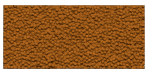	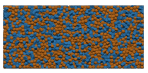	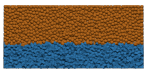	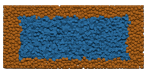	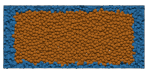
100% A (■)	100% B (■)	50% A (■) 50% B (■)	50% A (■) 50% B (■)	50% A (■) 50% B (■)	50% A (■) 50% B (■)

Applied pressure during consolidation. All six tablets are compacted to six different levels of consolidation given by $\rho_{\max}^{\text{in-die}} = [0.751, 0.805, 0.854, 0.904, 0.952, 0.998]$, unloaded and ejected from the die. The compaction process is dominated by plastic deformations and formation of solid bridges, while the unloading stage is characterized by elastic recovery and breakage of bonded surfaces. The numerical simulation accounts for these different physical mechanisms and it successfully predicts a residual radial stress after unloading [50]. Figure 12 shows predictions of pressure applied by the punches and reaction at the die wall for all six tablets during consolidation—thus the process-based nature of the proposed PNM construction. It is evident from the figure that the applied pressure is not only a function of the material properties and composition, but also of the topology of the microstructure. The elastic recovery during unloading, in contrast, is not significantly affected by material properties, composition and topology. It is interesting to note that the residual radial stress is different for different microstructural arrangements, which suggests that the tensile strength of these compacts is also a function of not only composition but also of the topology of the network of solid bridges.

Internal distribution of relative density or porosity. Pore space is intrinsically linked to packing density. Therefore, we examine the internal distribution of relative density or, its complement, porosity in all six tablet formulations studied in this section. We limit the analysis to one cross-section for each compact, at in-die relative density equal to 0.904. The local relative density is defined as the ratio between volume of a particle and volume of its Voronoi cell. The local porosity is defined as one minus the local relative density. For boundary particles of an unloaded and ejected compact, however, local density is highly dependent on the placement of walls during tesselation. Here, we position top and bottom flat surfaces, and lateral cylindrical surface, at an average position among all elastically recovered contact interfaces between particles and punch or die surfaces – the elastic recovery of each surface particle is different in general. Figure 13 illustrates these results. It is evident from the figure that the internal relative density distribution of tablets TA and TB are identical. However, all four 50-50 mixtures have distinctly different internal distributions of relative density due to different topological arrangements of compliant (i.e., materlal A) and stiff (i.e., material B) particles. These results highlight the importance of accounting for microstructural features in granular assemblies under large plastic deformations and, thus, of accouting for the consolidation process when studying phenomena occurring at the pore scale.

Pore-space statistical signature. The evolution of pore-space features during consolidation was

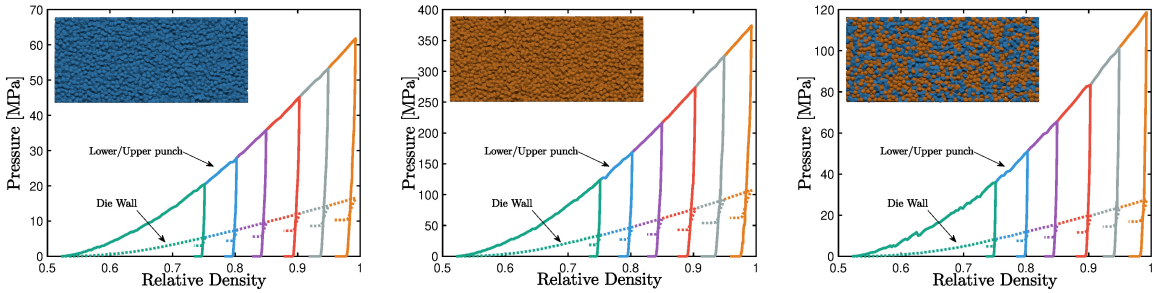

(a) TA tablet. (b) TB tablet. (c) TRAB tablet.

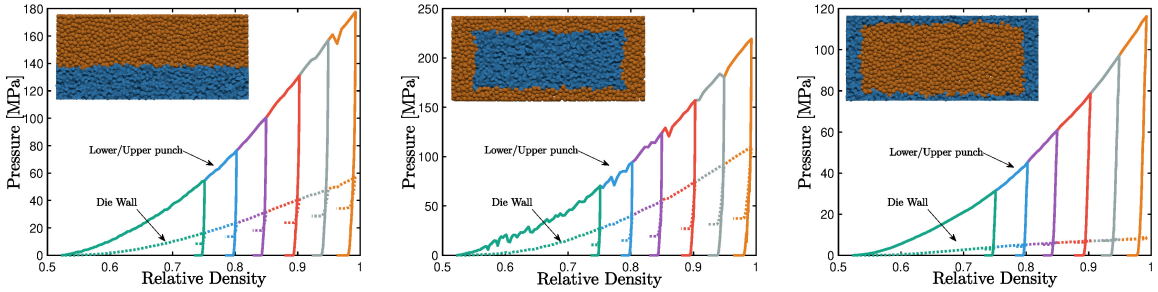

(d) THAB tablet. (e) TCASB tablet. (f) TCBSA tablet.

Figure 12: Punch and die-wall pressures as a function of relative density for tablets unloaded at six different levels of consolidation $\rho_{\max}^{\text{in-die}} = [0.751, 0.805, 0.854, 0.904, 0.952, 0.998]$.

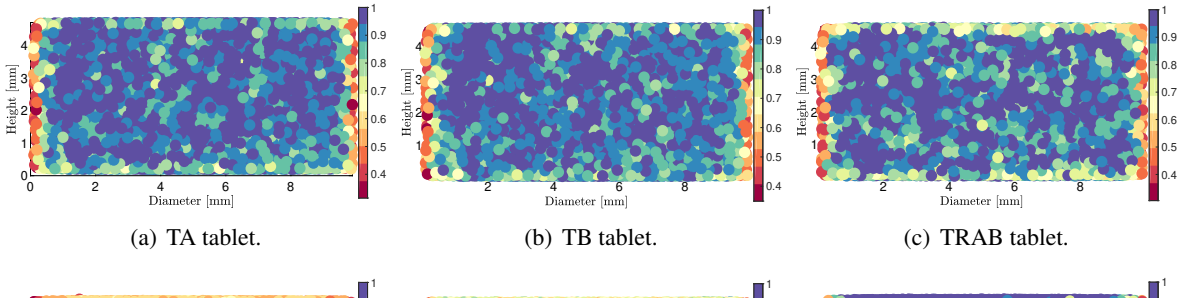

(a) TA tablet. (b) TB tablet. (c) TRAB tablet.

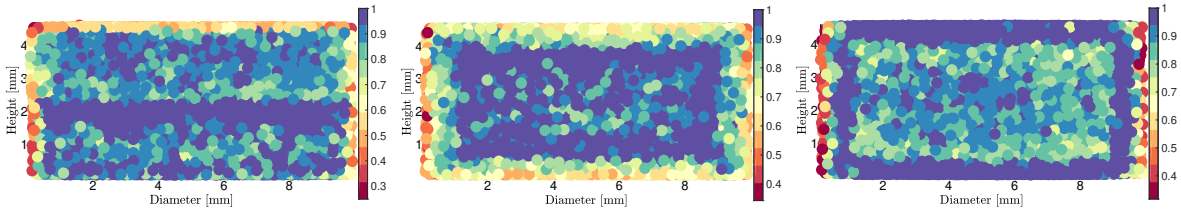

(d) THAB tablet. (e) TCASB tablet. (f) TCBSA tablet.

Figure 13: Internal distribution of relative density for tablets consolidated at a relative density of 0.904, unloaded and ejected from the die.

presented in Section 4.1 for tablet TA (see Figure 11). Here, Figures 14, 15, 16, and 17 show the probability density function of the pore-elements length, surface area, volume, cross-section area and shape factor, at five different in-die relative densities and for all four 50-50 mixtures (i.e., for tablets TRAB, THAB, TCASB and TCBSA). It is evident from the figure that (i) the distribution of surface area and shape factor are highly dependent of tablet topology, while following the same trend observed for tablet TA (i.e., they become narrower and skewed towards small values as relative density increases), (ii) the distribution of length is independent of tablet topology and thus it follows the same trend observed for tablet TA (i.e., it does not significantly change during consolidation), (iii) the distribution of cross-sectional area is uniquely different for TCBSA but, otherwise, it follows the same trend observed for TA (i.e., it remains wide, spanning two orders of magnitude, and shifts towards small values as relative density increases), and (iv) the distribution of volume is mostly independent of tablet topology and it becomes increasingly skewed and shifted towards small values, spanning two orders of magnitude, during consolidation. It bears emphasis that the permeability of each pore element depends nonlinearly on L_t, S_t, V_t, A_t and G_t (see equation (9)) which, in turn, not only depend on microstructural composition and effective porosity but, perhaps more importantly, on their spacial distribution within the microstructure, as this work reveals that they depend on topology and span orders of magnitude. Therefore, process-based approaches for constructing PNM are of paramount relevance to understanding architectured granular material systems.

Effective permeability. If pore-scale inertial forces are small compared to viscous forces, i.e., if $\mathrm{Re} \ll 1$, then conservation of mass for the Stokes flow is given by the following system of linear equations

$$\sum_{\{\upsilon_m,\upsilon_n\}\in I_1(\upsilon_m)} K_{mn}\,(P_m - P_n) = 0 \qquad \text{for all pores } \upsilon_m \tag{6}$$

where $\{\upsilon_m, \upsilon_n\}$ is a throat incident to pore υ_m, i.e., a throat in $I_1(\upsilon_m)$, K_{mn} is the conductance of throat $\{\upsilon_m, \upsilon_n\}$, and P_m is the pressure at pore υ_m. We calculate pore pressures for a differential pressure $\Delta P = 101,325$ Pa applied between top and bottom tablet surfaces. We next determine the ratio between effective permeability κ and fluid viscosity μ from [85]

$$\kappa/\mu = \frac{H_{\text{tablet}}}{A_{\text{tablet}}} \sum_{\upsilon_m\in\mathcal{B}_{\text{outlet}}} \sum_{\{\upsilon_m,\upsilon_n\}\in I_1(\upsilon_m)} K_{mn}\frac{P_m - P_n}{\Delta P} \tag{7}$$

where A_{tablet} and H_{tablet} are the compact cross-sectional area and thickness, respectively, and $\mathcal{B}_{\text{outlet}}$ is the set of pores located at the flow outlet, i.e., at the top surface of the tablet for a positive pressure differential. Figure 18 shows the effective permeability for all the tablets listed in Table 4 after being compacted, unloaded and ejected at different in-die relative densities. It is evident from the figure that there is a decreasing trend with decreasing porosity, or increasing relative density, in agreement with experimental evidence [90, 3]. However, the rank order among topologically different 50-50 mixtures can only be estimated from the process-based PNM construction proposed in this work. Specifically, for these packings of spherical particles of equal size, these differences are most evident at relative densities under 0.85, which are values often used in pharmaceutical and pre-sintered ceramic products. Furthermore, it is interesting to observe that tablets TA and TB, i.e., tablets composed of 100% material A and 100% material B, respectively, have different values of effective permeability due to a different elastic recovery of the microstructure during unloading and ejection. The systematic investigation of these trends with the proposed process-based PNM construction and their experimental validation are worthwhile directions of future research.

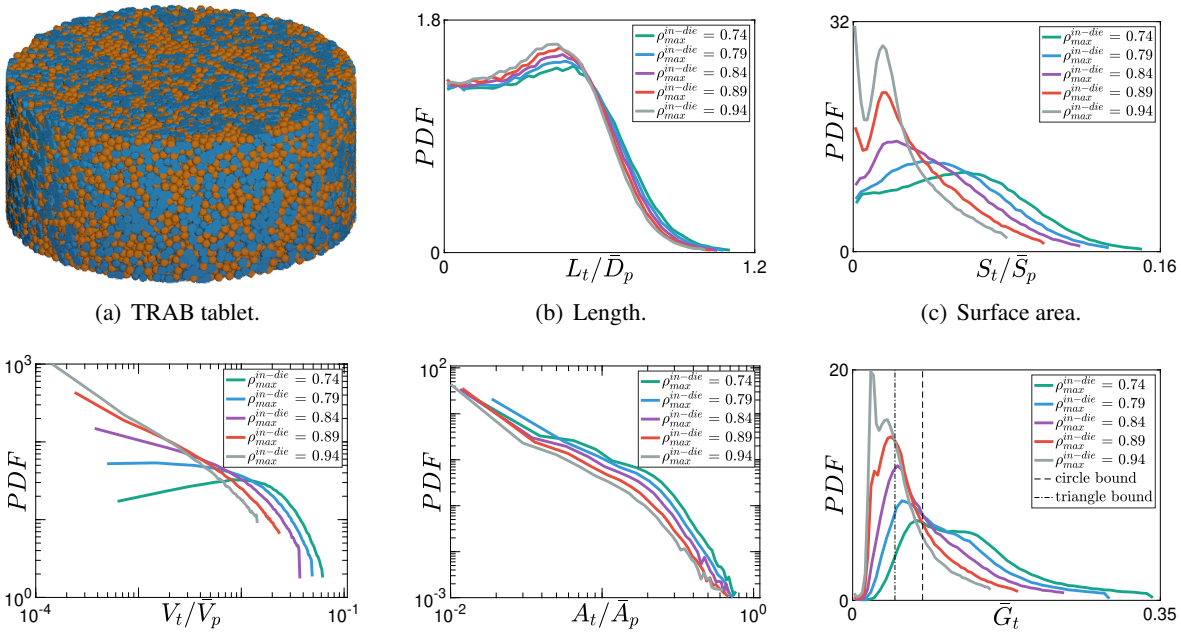

(a) TRAB tablet. (b) Length. (c) Surface area.

(d) Volume. (e) Cross-sectional area. (f) Shape factor.

Figure 14: Pore-space statistical signature of the TRAB tablet.

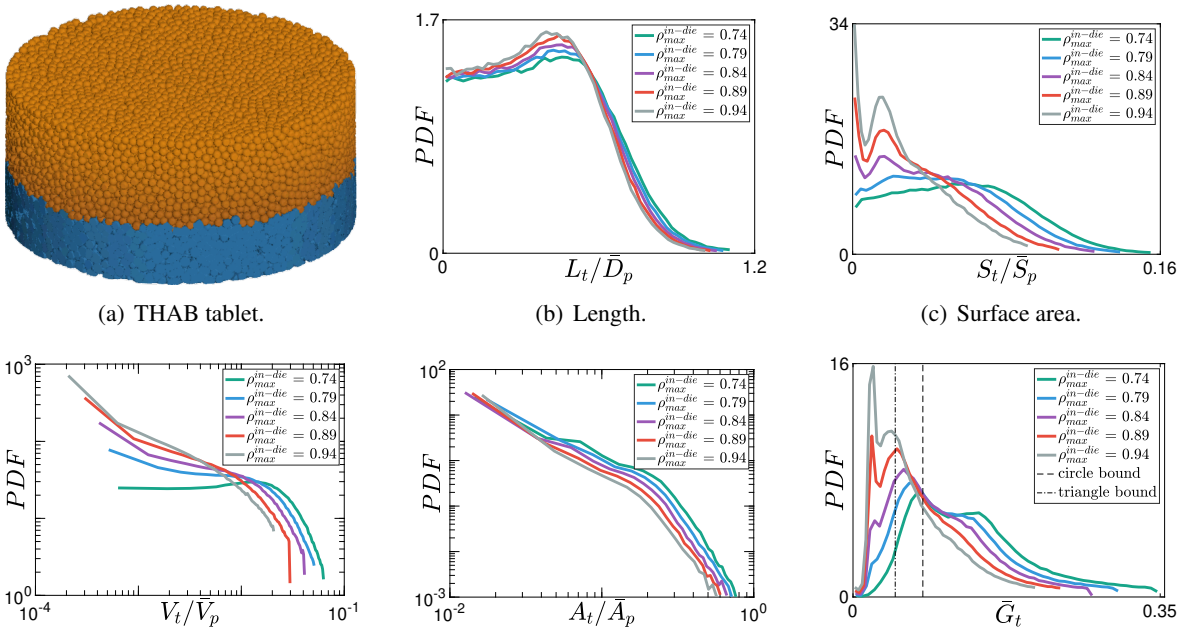

(a) THAB tablet. (b) Length. (c) Surface area.

(d) Volume. (e) Cross-section area. (f) Shape factor.

Figure 15: Pore-space statistical signature of the THAB tablet.

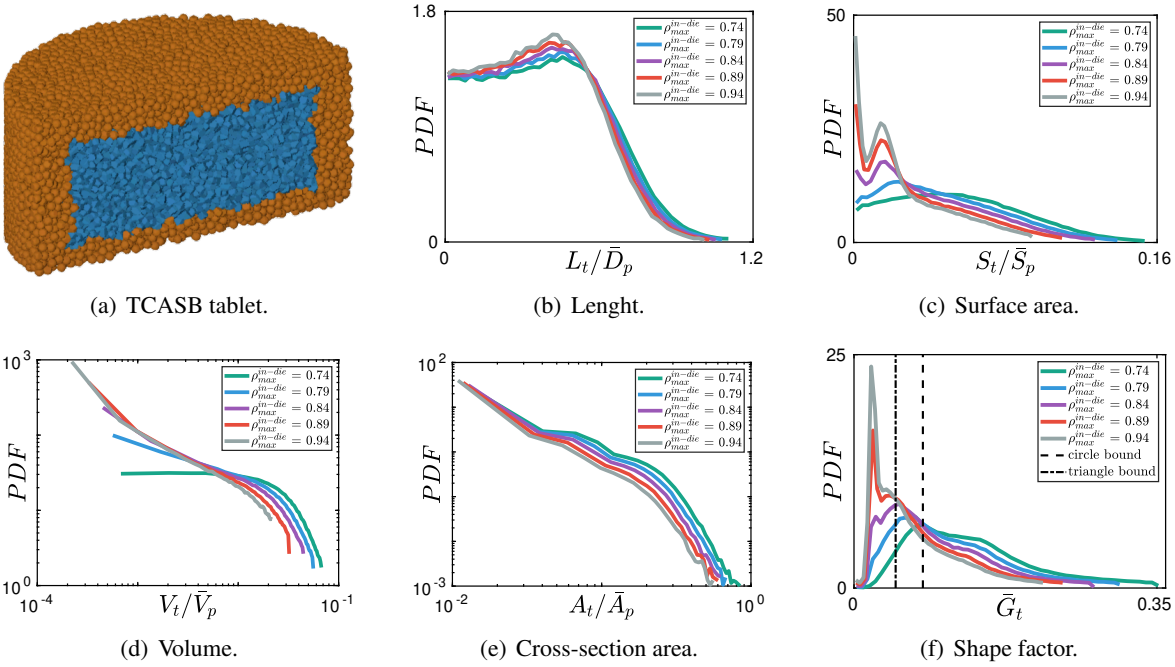

(a) TCASB tablet. (b) Lenght. (c) Surface area.

(d) Volume. (e) Cross-section area. (f) Shape factor.

Figure 16: Pore-space statistical signature of the TCASB tablet.

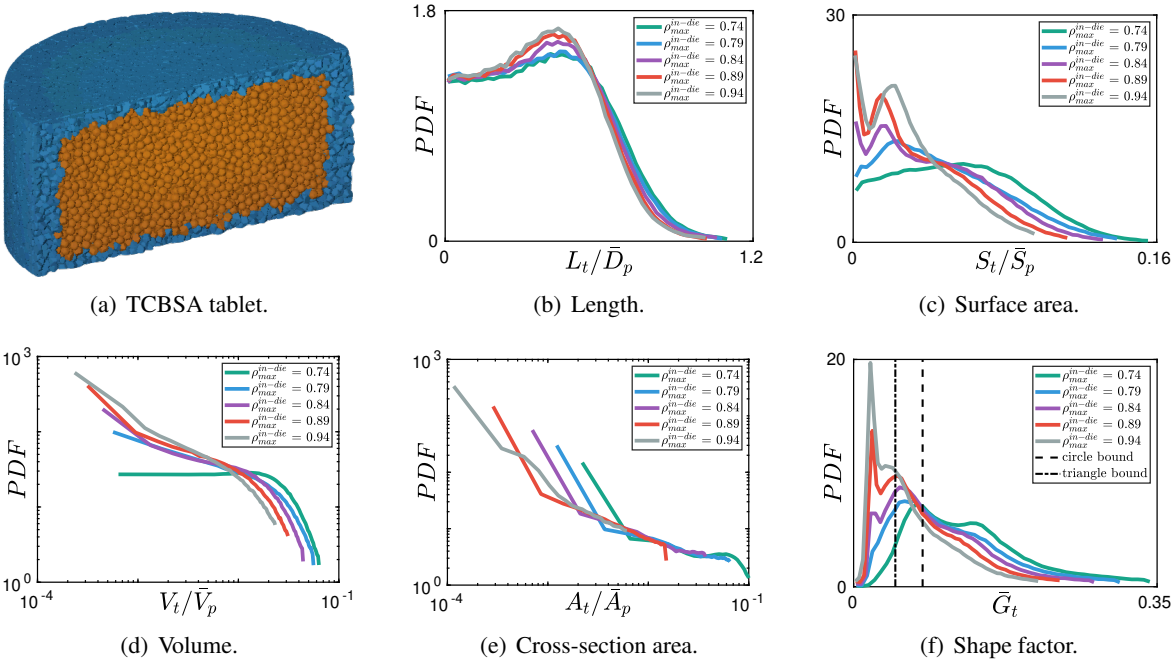

(a) TCBSA tablet. (b) Length. (c) Surface area.

(d) Volume. (e) Cross-section area. (f) Shape factor.

Figure 17: Pore-space statistical signature of the TCBSA tablet.

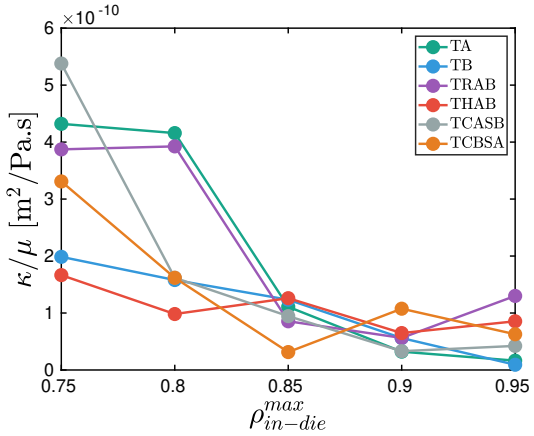

Figure 18: Effective permeability for all tablets listed in Table 4 under a pressure differential of $\Delta P = 101,325$ Pa between their top and bottom flat surfaces.

6 Concluding remarks

We have proposed a process-based method for constructing a pore network model of granular packings under large deformations. The method uses the radical Voronoi tessellation and CSG operations on meshes of deformed particles, to construct a three-dimensional solid of the pore network and estimate its geometric characteristics, CTS-model parameters and flow transport properties, and it uses the particle mechanics approach to model consolidation of powders under large deformations. Therefore, this process-based method explicitly simulates not only a packing of grains but also its corresponding consolidation process. We have specifically restricted attention to powder die compaction processes, i.e., to die filling, compaction to low porosity values, unloading, and ejection.

We have exemplified the efficacy of the proposed process-based PNM construction by studying granular packings with the same composition, namely a 50-50 binary mixture of two monodisperse systems comprised by elasto-plastic spheres with bonding strength, but with microstructures which are topologically different, namely a random packing, a bilayer, and core-shell structures. These simulations reveal the evolution, up to relative densities close to one, of (i) the applied pressure during consolidation, (ii) the internal distribution of relative density, and (iii) the pore space statistical signature, i.e., the probability density function of the pore-elements length, surface area, volume, cross-section area and shape factor. It is evident that the topological differences affect both the microstructural response and the macroscopic behavior. The compaction curves and density internal distributions are different for all four studied formulations, although their composition is the same. Furthermore, the consolidation process leaves a clear signature in the pore space. Specifically, it is observed that (i) the distribution of surface area and shape factor are highly dependent of tablet topology, while following the general trend of becoming narrower and skewed towards small values as relative density increases (i.e., cross-sections transition from circular to triangular), (ii) the distribution of length is independent of tablet topology and it does not significantly change during consolidation, (iii) the distribution of cross-sectional area is uniquely different for one of the core-shell tablets (soft shell and hard core) but, otherwise, it follows the general trend of remaining wide (spanning two orders of magnitude) and shifting towards small values as relative density increases, and (iv) the distribution of volume is mostly independent of tablet topology and it becomes increasingly skewed and shifted towards small values, spanning two orders of magnitude, during consolidation. It bears emphasis that the permeability of each pore element depends nonlinearly on these geometric parameters

and, therefore, the effective permeability of the system depends not only on microstructural composition and effective porosity but, perhaps more importantly, on the topological arrangement of their components. Therefore, this work showcases that process-based approaches for constructing PNM are of paramount relevance to understanding architectured granular material systems.

Acknowledgments

The authors gratefully acknowledges the support received from the National Science Foundation grant number CMMI-1538861.

References

[1] Daniel Markl, Alexa Strobel, Rüdiger Schlossnikl, Johan Bøtker, Prince Bawuah, Cathy Ridgway, Jukka Rantanen, Thomas Rades, Patrick Gane, Kai-Erik Peiponen, et al. Characterisation of pore structures of pharmaceutical tablets: A review. *International journal of pharmaceutics*, 538(1-2):188–214, 2018. doi: https://doi.org/10.1016/j.ijpharm.2018.01.017.

[2] Qingrong Xiong, Todor G Baychev, and Andrey P Jivkov. Review of pore network modelling of porous media: experimental characterisations, network constructions and applications to reactive transport. *Journal of contaminant hydrology*, 192:101–117, 2016. doi: 10.1016/j.jconhyd.2016.07.002.

[3] Martin J Blunt. *Multiphase flow in permeable media: A pore-scale perspective*. Cambridge University Press, 2017. doi: 10.1017/9781316145098.

[4] Veerle Cnudde and Matthieu Nicolaas Boone. High-resolution x-ray computed tomography in geosciences: A review of the current technology and applications. *Earth-Science Reviews*, 123: 1–17, 2013. doi: 10.1016/j.earscirev.2013.04.003.

[5] Dorthe Wildenschild and Adrian P Sheppard. X-ray imaging and analysis techniques for quantifying pore-scale structure and processes in subsurface porous medium systems. *Advances in Water Resources*, 51:217–246, 2013. doi: 10.1016/j.advwatres.2012.07.018.

[6] Steffen Schlüter, Adrian Sheppard, Kendra Brown, and Dorthe Wildenschild. Image processing of multiphase images obtained via x-ray microtomography: a review. *Water Resources Research*, 50(4):3615–3639, 2014. doi: 10.1002/2014wr015256.

[7] Mark Erman Curtis, Raymond Joseph Ambrose, Carl H Sondergeld, et al. Structural characterization of gas shales on the micro-and nano-scales. In *Canadian unconventional resources and international petroleum conference*. Society of Petroleum Engineers, 2010. doi: 10.2118/137693-ms.

[8] Herman Lemmens, Alan Butcher, PW Botha, et al. Fib/sem and automated mineralogy for core and cuttings analysis. In *SPE Russian Oil and Gas Conference and Exhibition*. Society of Petroleum Engineers, 2010. doi: 10.2118/136327-ms.

[9] Liviu Tomutsa, Dmitriy Borisovich Silin, Velimir Radmilovic, et al. Analysis of chalk petrophysical properties by means of submicron-scale pore imaging and modeling. *SPE Reservoir Evaluation & Engineering*, 10(03):285–293, 2007. doi: 10.2118/99558-pa.

[10] Robert M Sok, Mark A Knackstedt, Trond Varslot, Abid Ghous, Shane Latham, Adrian P Sheppard, et al. Pore scale characterization of carbonates at multiple scales: Integration of micro-ct, bsem, and fibsem. *Petrophysics*, 51(06), 2010.

[11] Bernhard Blümich, Federico Casanova, and Stephan Appelt. Nmr at low magnetic fields. *Chemical Physics Letters*, 477(4-6):231–240, 2009. doi: 10.1016/j.cplett.2009.06.096.

[12] Paul T. Callaghan. *Principles of nuclear magnetic resonance microscopy*. Oxford University Press on Demand, 1993.

[13] PM Adler and J-F Thovert. Real porous media: Local geometry and macroscopic properties. *Applied Mechanics Reviews*, 51(9):537–585, 1998. doi: 10.1115/1.3099022.

[14] Pierre Adler. *Porous media: geometry and transports*. Elsevier, 2013.

[15] CLY Yeong and Salvatore Torquato. Reconstructing random media. *Physical Review E*, 57(1): 495, 1998. doi: 10.1103/physreve.57.495.

[16] CLY Yeong and SJPRE Torquato. Reconstructing random media. ii. three-dimensional media from two-dimensional cuts. *Physical Review E*, 58(1):224, 1998. doi: 10.1103/physreve.58.224.

[17] R Hilfer. Geometric and dielectric characterization of porous media. *Physical Review B*, 44(1): 60, 1991. doi: 10.1103/physrevb.44.60.

[18] David A Coker, Salvatore Torquato, and John H Dunsmuir. Morphology and physical properties of fontainebleau sandstone via a tomographic analysis. *Journal of Geophysical Research: Solid Earth*, 101(B8):17497–17506, 1996. doi: 10.1029/96jb00811.

[19] RD Hazlett. Statistical characterization and stochastic modeling of pore networks in relation to fluid flow. *Mathematical geology*, 29(6):801–822, 1997. doi: 10.1007/bf02768903.

[20] C Manwart, Salvatore Torquato, and R Hilfer. Stochastic reconstruction of sandstones. *Physical Review E*, 62(1):893, 2000. doi: 10.1103/physreve.62.893.

[21] Hiroshi Okabe and Martin J Blunt. Prediction of permeability for porous media reconstructed using multiple-point statistics. *Physical Review E*, 70(6):066135, 2004. doi: 10.1103/physreve.70.066135.

[22] Hiroshi Okabe and Martin J Blunt. Pore space reconstruction using multiple-point statistics. *Journal of Petroleum Science and Engineering*, 46(1-2):121–137, 2005. doi: 10.1016/j.petrol.2004.08.002.

[23] W Brent Lindquist, Sang-Moon Lee, David A Coker, Keith W Jones, and Per Spanne. Medial axis analysis of void structure in three-dimensional tomographic images of porous media. *Journal of Geophysical Research: Solid Earth*, 101(B4):8297–8310, 1996. doi: 10.1029/95jb03039.

[24] W Brent Lindquist, Arun Venkatarangan, John Dunsmuir, and Teng-fong Wong. Pore and throat size distributions measured from synchrotron x-ray tomographic images of fontainebleau sandstones. *Journal of Geophysical Research: Solid Earth*, 105(B9):21509–21527, 2000. doi: 10.1029/2000jb900208.

[25] Riyadh Al-Raoush, Karsten Thompson, and Clinton S Willson. Comparison of network generation techniques for unconsolidated porous media. *Soil Science Society of America Journal*, 67 (6):1687–1700, 2003. doi: 10.2136/sssaj2003.1687.

[26] RI Al-Raoush and CS Willson. Extraction of physically realistic pore network properties from three-dimensional synchrotron x-ray microtomography images of unconsolidated porous media systems. *Journal of hydrology*, 300(1-4):44–64, 2005. doi: 10.1016/j.jhydrol.2004.05.005.

[27] Dmitriy Silin and Tad Patzek. Pore space morphology analysis using maximal inscribed spheres. *Physica A: Statistical mechanics and its applications*, 371(2):336–360, 2006. doi: 10.1016/j.physa.2006.04.048.

[28] Mohammad Piri and Martin J Blunt. Three-dimensional mixed-wet random pore-scale network modeling of two-and three-phase flow in porous media. i. model description. *Physical Review E*, 71(2):026301, 2005. doi: 10.1103/physreve.71.026301.

[29] V Mourzenko, J-F Thovert, O Vizika, and PM Adler. Geometrical and transport properties of random packings of polydisperse spheres. *Physical Review E*, 77(6):066306, 2008. doi: 10.1103/physreve.77.066306.

[30] Steven L Bryant, David W Mellor, and Christopher A Cade. Physically representative network models of transport in porous media. *AIChE Journal*, 39(3):387–396, 1993. doi: 10.1002/aic.690390303.

[31] Steven L Bryant, Peter R King, and David W Mellor. Network model evaluation of permeability and spatial correlation in a real random sphere packing. *Transport in porous media*, 11(1):53–70, 1993. doi: 10.1007/bf00614635.

[32] Stig Bakke, Pål-Eric Øren, et al. 3-d pore-scale modelling of sandstones and flow simulations in the pore networks. *Spe Journal*, 2(02):136–149, 1997. doi: 10.2118/35479-pa.

[33] Pål-Eric Øren and Stig Bakke. Process based reconstruction of sandstones and prediction of transport properties. *Transport in porous media*, 46(2-3):311–343, 2002. doi: 10.1023/A:1015031122338.

[34] B Biswal, C Manwart, R Hilfer, S Bakke, and PE Øren. Quantitative analysis of experimental and synthetic microstructures for sedimentary rock. *Physica A: Statistical Mechanics and its Applications*, 273(3-4):452–475, 1999. doi: 10.1016/s0378-4371(99)00248-4.

[35] B Biswal, RJ Held, V Khanna, J Wang, and R Hilfer. Towards precise prediction of transport properties from synthetic computer tomography of reconstructed porous media. *Physical Review E*, 80(4):041301, 2009. doi: 10.1103/PhysRevE.80.041301.

[36] Bruno Chareyre, Andrea Cortis, Emanuele Catalano, and Eric Barthélemy. Pore-scale modeling of viscous flow and induced forces in dense sphere packings. *Transport in porous media*, 94(2):595–615, 2012. doi: 10.1007/s11242-012-0057-2.

[37] Herbert Edelsbrunner and Nimish R Shah. Incremental topological flipping works for regular triangulations. *Algorithmica*, 15(3):223–241, 1996. doi: 10.1007/bf01975867.

[38] AP Sheppard, RM Sok, H Averdunk, VB Robins, and A Ghous. Analysis of rock microstructure using high-resolution x-ray tomography. In *Proceedings of the International Symposium of the Society of Core Analysts*, pages 1–12, 2006.

[39] M. E. J. Newman. *Networks: an introduction*. Oxford University Press, Oxford; New York, 2010. ISBN 9780199206650 0199206651.

[40] Joost H van der Linden, Adnan Sufian, Guillermo A Narsilio, Adrian R Russell, and Antoinette Tordesillas. A computational geometry approach to pore network construction for granular packings. *Computers & geosciences*, 112:133–143, 2018. doi: https://doi.org/10.1016/j.cageo.2017.12.004.

[41] Fabian M Schaller, Sebastian C Kapfer, Myfanwy E Evans, Matthias JF Hoffmann, Tomaso Aste, Mohammad Saadatfar, Klaus Mecke, Gary W Delaney, and Gerd E Schröder-Turk. Set voronoi diagrams of 3d assemblies of aspherical particles. *Philosophical Magazine*, 93(31-33):3993–4017, 2013. doi: 10.1080/14786435.2013.834389.

[42] Simon Weis, Philipp WA Schönhöfer, Fabian M Schaller, Matthias Schröter, and Gerd E Schröder-Turk. Pomelo, a tool for computing generic set voronoi diagrams of aspherical particles of arbitrary shape. In *EPJ Web of Conferences*, volume 140, page 06007. EDP Sciences, 2017.

[43] L Burtseva and F Werner. Using mathematical tessellation to model spherical particle packing structures. *International Journal of Mathematics, Game Theory and Algebra*, 24:2–3, 2015.

[44] Anne Poupon. Voronoi and voronoi-related tessellations in studies of protein structure and interaction. *Current opinion in structural biology*, 14(2):233–241, 2004. doi: 10.1016/j.sbi.2004.03.010.

[45] C. H. Rycroft. Voro++: A three-dimensional voronoi cell library in c++. *Chaos: An Interdisciplinary Journal of Nonlinear Science*, 19:041111, 2009. doi: 10.2172/946741.

[46] Marcial Gonzalez and Alberto M Cuitiño. A nonlocal contact formulation for confined granular systems. *Journal of the Mechanics and Physics of Solids*, 60(2):333–350, 2012.

[47] Marcial Gonzalez and Alberto M Cuitiño. Microstructure evolution of compressible granular systems under large deformations. *Journal of the Mechanics and Physics of Solids*, 93:44–56, 2016. doi: 10.1016/j.jmps.2016.03.024.

[48] B Yohannes, M Gonzalez, A Abebe, O Sprockel, F Nikfar, S Kiang, and AM Cuitiño. Evolution of the microstructure during the process of consolidation and bonding in soft granular solids. *International journal of pharmaceutics*, 503(1-2):68–77, 2016.

[49] B Yohannes, M Gonzalez, A Abebe, O Sprockel, F Nikfar, S Kiang, and AM Cuitiño. Discrete particle modeling and micromechanical characterization of bilayer tablet compaction. *International journal of pharmaceutics*, 529(1-2):597–607, 2017.

[50] Marcial Gonzalez. Generalized loading-unloading contact laws for elasto-plastic spheres with bonding strength. *Journal of the Mechanics and Physics of Solids*, 122:633–656, 2019. doi: https://doi.org/10.1016/j.jmps.2018.09.023.

[51] M Campen and L Kobbelt. Exact and robust (self-)intersections for polygonal meshes. *Comput. Graph. Forum*, 29(2):397–406, 2010. doi: 10.1111/j.1467-8659.2009.01609.x.

[52] F R Feito, C J Ogayar, R J Segura, and M L Rivero. Fast and accurate evaluation of regularized boolean operations on triangulated solids. *Cad Comput. Aided Design*, 45(3):705–716, 2013. doi: 10.1016/j.cad.2012.11.004.

[53] P Hachenberger and L Kettner. *3D Boolean operations on Nef polyhedra, CGAL User and Reference Manual 3.9*. CGAL Editorial Board, 2011.

[54] M Douze, J-S Franco, and B Raffin. *QuickCSG: Arbitrary and Faster Boolean Combinations of n Solids*. PhD thesis, Inria-Research Centre Grenoble–Rhône-Alpesl, INRIA, 2015.

[55] Qingnan Zhou, Eitan Grinspun, Denis Zorin, and Alec Jacobson. Mesh arrangements for solid geometry. *ACM Transactions on Graphics (TOG)*, 35(4):1–15, 2016.

[56] B Sheng, P Li, H Fuc, L Ma, and E Wud. Efficient non-incremental constructive solid geometry evaluation for triangular meshes. *Graphical Models*, 97:1–16, 2018. doi: 10.1016/j.gmod.2018.03.001.

[57] M Panfilov and I Panfilova. Phenomenological meniscus model for two-phase flows in porous media. *Transport in porous media*, 58(1-2):87–119, 2005. doi: 10.1007/s11242-004-5471-7.

[58] Eyvind Aker, Knut Jørgen Måløy, Alex Hansen, and G George Batrouni. A two-dimensional network simulator for two-phase flow in porous media. *Transport in porous media*, 32(2):163–186, 1998. doi: 10.1023/A:1006510106194.

[59] Helge K Dahle and Michael A Celia. A dynamic network model for two-phase immiscible flow. *Computational Geosciences*, 3(1):1–22, 1999. doi: 10.1023/A:1011522808132.

[60] Rachid Hannaoui, Pierre Horgue, Faical Larachi, Yacine Haroun, Frédéric Augier, Michel Quintard, and Marc Prat. Pore-network modeling of trickle bed reactors: Pressure drop analysis. *Chemical Engineering Journal*, 262:334–343, 2015. doi: 10.1016/j.cej.2014.09.098.

[61] J Koplik, TJ Lasseter, et al. Two-phase flow in random network models of porous media. *Society of Petroleum Engineers Journal*, 25(01):89–100, 1985. doi: 10.2118/11014-pa.

[62] Mohammed S Al-Gharbi and Martin J Blunt. Dynamic network modeling of two-phase drainage in porous media. *Physical Review E*, 71(1):016308, 2005. doi: 10.1103/physreve.71.016308.

[63] TW Patzek and DB Silin. Shape factor and hydraulic conductance in noncircular capillaries: I. one-phase creeping flow. *Journal of colloid and interface science*, 236(2):295–304, 2001. doi: 10.1006/jcis.2000.7413.

[64] AV Ryazanov, Marinus Izaak Jan Van Dijke, and Kenneth Stuart Sorbie. Two-phase pore-network modelling: existence of oil layers during water invasion. *Transport in Porous Media*, 80(1):79–99, 2009. doi: 10.1007/s11242-009-9345-x.

[65] Frouke Hoogland, Peter Lehmann, Rajmund Mokso, and Dani Or. Drainage mechanisms in porous media: From piston-like invasion to formation of corner flow networks. *Water Resources Research*, 52(11):8413–8436, 2016. doi: 10.1002/2016wr019299.

[66] HN Man and XD Jing. Pore network modelling of electrical resistivity and capillary pressure characteristics. *Transport in Porous Media*, 41(3):263–285, 2000. doi: 10.1023/A:1006612100346.

[67] V Joekar-Niasar, M Prodanović, D Wildenschild, and SM Hassanizadeh. Network model investigation of interfacial area, capillary pressure and saturation relationships in granular porous media. *Water Resources Research*, 46(6), 2010. doi: 10.1029/2009wr008585.

[68] Marcelo Lago and Mariela Araujo. Threshold pressure in capillaries with polygonal cross section. *Journal of colloid and interface science*, 243(1):219–226, 2001. doi: 10.1006/jcis.2001.7872.

[69] Ali Q Raeini, Branko Bijeljic, and Martin J Blunt. Generalized network modeling of capillary-dominated two-phase flow. *Physical Review E*, 97(2):023308, 2018. doi: 10.1103/physreve.97.023308.

[70] Christer Nyström, Göran Alderborn, Margareta Duberg, and Per-Gunnar Karehill. Bonding surface area and bonding mechanism-two important factors fir the understanding of powder comparability. *Drug development and industrial pharmacy*, 19(17-18):2143–2196, 1993. doi: 10.3109/03639049309047189.

[71] Goran Alderborn and Christer Nystrom. *Pharmaceutical Powder ComPattion Technology*. CRC Press, 1995.

[72] Jianhua Zhou, Yuwen Zhang, and JK Chen. Numerical simulation of random packing of spherical particles for powder-based additive manufacturing. *Journal of manufacturing science and engineering*, 131(3):031004, 2009. doi: 10.1115/1.3123324.

[73] LF Liu, ZP Zhang, and AB Yu. Dynamic simulation of the centripetal packing of mono-sized spheres. *Physica A: Statistical Mechanics and its Applications*, 268(3-4):433–453, 1999. doi: 10.1016/s0378-4371(99)00106-5.

[74] YF Cheng, SJ Guo, and HY Lai. Dynamic simulation of random packing of spherical particles. *Powder Technology*, 107(1-2):123–130, 2000. doi: 10.1016/s0032-5910(99)00178-3.

[75] Ankit Agarwal and Marcial Gonzalez. Contact radius and curvature corrections to the nonlocal contact formulation accounting for multi-particle interactions in elastic confined granular systems. *International Journal of Engineering Science*, 133:26–46, 2018.

[76] Bertil Storåkers, Shiro Biwa, and Per-Lennart Larsson. Similarity analysis of inelastic contact. *International Journal of Solids and Structures*, 34(24):3061–3083, 1997. doi: 10.1016/s0020-7683(96)00176-x.

[77] Erik Olsson and P-L Larsson. On force–displacement relations at contact between elastic–plastic adhesive bodies. *Journal of the Mechanics and Physics of Solids*, 61(5):1185–1201, 2013.

[78] Atsuyuki Okabe, Barry Boots, Kokichi Sugihara, and Sung Nok Chiu. *Spatial tessellations: concepts and applications of Voronoi diagrams*, volume 501. John Wiley & Sons, 2009.

[79] Allen Hatcher. *Algebraic Topology*. Cambridge University Press, 2002.

[80] Alec Jacobson et al. gptoolbox: Geometry processing toolbox, 2018. URL https://github.com/alecjacobson/gptoolbox. http://github.com/alecjacobson/gptoolbox.

[81] David Legland et al. MatGeom: Matlab geometry toolbox for 2d/3d geometric computing, 2018. URL https://github.com/mattools/matGeom. https://github.com/mattools/matGeom.

[82] Sonia M Razavi, Marcial Gonzalez, and Alberto M Cuitiño. Quantification of lubrication and particle size distribution effects on tensile strength and stiffness of tablets. *Powder Technology*, 336:360–374, 2018. doi: 10.1016/j.powtec.2018.06.001.

[83] P. E. Øren, S. Bakke, and O. J. Arntzen. Extending predictive capabilities to network models. *SPE journal*, 3(04):324–336, 1998. doi: 10.2118/52052-pa.

[84] Martin J Blunt. Physically-based network modeling of multiphase flow in intermediate-wet porous media. *Journal of Petroleum Science and Engineering*, 20(3-4):117–125, 1998. doi: 10.1016/s0920-4105(98)00010-2.

[85] Jacob Bear. *Dynamics of fluids in porous media*. Courier Corporation, 2013.

[86] David P Doane. Aesthetic frequency classifications. *The American Statistician*, 30(4):181–183, 1976. doi: 10.2307/2683757.

[87] Admassu Abebe, Ilgaz Akseli, Omar Sprockel, Niranjan Kottala, and Alberto M Cuitiño. Review of bilayer tablet technology. *International journal of pharmaceutics*, 461(1-2):549–558, 2014.

[88] Foad Mahmoodi, Ingvild Klevan, Josefina Nordström, Göran Alderborn, and Göran Frenning. A comparison between two powder compaction parameters of plasticity: The effective medium a parameter and the heckel 1/k parameter. *International journal of pharmaceutics*, 453(2):295–299, 2013. doi: 10.1016/j.ijpharm.2013.06.040.

[89] Renato Panelli and Francisco Ambrozio Filho. A study of a new phenomenological compacting equation. *Powder Technology*, 114(1-3):255–261, 2001. doi: 10.1016/s0032-5910(00)00207-2.

[90] Christoph H Arns, Mark A Knackstedt, W Val Pinczewski, and Nicos S Martys. Virtual permeametry on microtomographic images. *Journal of Petroleum Science and Engineering*, 45(1-2): 41–46, 2004.